## EDGE ARTICLE

Check for updates

All publication charges for this article have been paid for by the Royal Society of Chemistry

# Tailoring electrolyte coordination structure for high-rate polymer-based solid-state batteries

Zexi Wang,[a] Zhencheng Huang,[a] Hao Guo, [b] Tao Huang,[ac] Jingguo Gao,[acd] Junzheng Lai,[ac] Na Feng,[ac] Ziqi Wang, [e] Xuming Yang,[ac] Yongliang Li, [a] Jianhong Liu,[ac] Yi Wang,*[a] Qianling Zhang, [acd] Jiangtao Hu [*acd] and Xiangzhong Ren [*a]

Solid-state batteries (SSBs) offer intrinsic safety and superior energy density, promising next-generation energy storage. Polymer-based solid-state electrolytes (SSEs) stand out for their facile processing and low cost. However, the development of SSBs is impeded by the intrinsically low ionic conductivity of polymer electrolytes at room temperature, alongside limitations in their inherent electrochemical stability and thermal resilience. Here, we propose a novel solvation-tailoring strategy by embedding 3D continuously interconnected zirconium-based metal–organic framework (MOF808) nanofillers into a polyvinylidene fluoride–hexafluoropropylene (PVDF–HFP) matrix (designated as PLM-3). This design leverages the strong adsorption of MOF808 for solvent molecules ($-0.521$ eV) to thermodynamically displace them from the Li$^+$ solvation sheath, replacing them with anions and forming an anion-enriched coordination configuration. This precisely tailored solvation environment, quantified by a surge in anion-aggregate (AGG) species, significantly enhances Li$^+$ transport kinetics by reducing Li$^+$ desolvation energy by 15.8% ($-5.29$ *vs.* $-6.28$ eV), thereby endowing the resultant electrolyte with exceptional rate performance. When coupled with a high voltage single-crystal NCM83 (SC-NCM83) cathode, the PLM-3 cell delivers exceptional rate capability (219.5 mAh g$^{-1}$ at 0.1C; 182.8 mAh g$^{-1}$ at 5C) while maintaining 93.73% capacity retention after 200 cycles at 1C with a 4.3 V cutoff voltage. This solvation-tailoring strategy thus redefines the rate limits of polymer-based SSBs and paves the way for the development of high-power, high-energy, and industrially viable SSBs.

## Introduction

High-energy-density lithium (Li) batteries present critical safety hazards, including a propensity for combustion and explosion under thermal runaway conditions.[1–3] This risk is particularly pronounced in the presence of organic liquid electrolytes, which can act as primary fuel sources during failure events.[4,5] SSBs have emerged as a pivotal avenue in the pursuit of next-generation energy storage technologies, owing to their superior safety features and high energy density.[6–11] The SSEs stand

*[a]Shenzhen Key Laboratory of Functional Polymers, College of Chemistry and Environmental Engineering, Shenzhen University, Shenzhen, 518060, China. E-mail: wangyi0435@szu.edu.cn; hujt@szu.edu.cn; renxz@szu.edu.cn*

*[b]State Key Laboratory of Advanced Chemical Power Sources, Zunyi, Guizhou, 563003, China*

*[c]Graphene Composite Research Center, College of Chemistry and Environmental Engineering, Shenzhen University, Shenzhen, 518060, China*

*[d]State Key Laboratory of Intelligent Construction and Healthy Operation and Maintenance of Deep Underground Engineering, Shenzhen University, Shenzhen, 518060, China*

*[e]Department of Materials Science and Engineering, College of Materials Science, Jinan University, Guangzhou, 511443, China*

as a cornerstone component in SSBs, exerting a direct influence on battery performance and safety,[12–15] and are typically classified into three categories: inorganic solid electrolytes (ISEs), solid polymer electrolytes (SPEs), and composite polymer electrolytes (CPEs).[16] ISEs typically exhibit high room-temperature ionic conductivity and mechanical strength.[17] However, their match with Li metal anodes and high voltage SC-NCM83 cathodes is hindered by harsh processing requirements and poor electrochemical stability. In contrast, SPEs have desirable elasticity and toughness for optimal interfacial contact, as well as excellent processability for large scale production.[4] However, their relatively poor ionic conductivity at room temperature and lower voltage tolerance, combined with kinetic barriers to ion transport and accelerated interfacial degradation,[18] collectively pose formidable obstacles to widespread adoption by severely compromising rate capability and long-term cycling stability.

To address these challenges, significant efforts have been pursued in both academic and industrial sectors, implementing strategies such as *in situ* polymerization,[19–22] incorporation of functional fillers,[23–25] and polymer matrix engineering.[26,27] Among these approaches, the introduction of functional fillers into SPEs to form CPEs has proven highly effective in

simultaneously enhancing ionic conductivity, reinforcing mechanical properties, and optimizing interfaces.[28–30] The introduced fillers can be inert materials, such as silicon dioxide $(SiO_2)$,[31] aluminum oxide $(Al_2O_3)$,[32] and graphitic carbon nitride $(g\text{-}C_3N_4)$.[33] These inert materials do not conduct $Li^+$. Their incorporation enhances amorphous domains within the polymer phase and reduces crystallinity, thereby elevating the ionic conductivity of CPEs. Moreover, these fillers can be active inorganic materials with ionic conductivity, such as $Li_7La_3Zr_2O_{12}$ with a garnet structure, $Li_{1+x}Al_xTi_{2-x}(PO_4)_3$ of the NASICON type, and $Li_{3x}La_{2/3-x}TiO_3$ with a perovskite structure.[34] These active fillers retain the general functions of inert fillers and increase the concentration of free $Li^+$ at the interface between the filler and the polymer matrix, thereby enhancing the overall ionic conductivity of CPEs. In addition to the above fillers, in recent years, some fillers with unique structures and rich functional groups have been reported, such as metal–organic frameworks (MOFs),[35] two dimensional (2D) materials,[36] and alloy fillers.[37] Building upon this paradigm, Luo et al.[38] incorporated porous $V_2O_5$ nanotubes (VNTs) into PVDF matrices, suppressing crystallinity and furnishing express $Li^+$ highways. The resultant electrolyte displays markedly elevated conductivity and robust interfacial kinetics, endowing full cells with enduring cyclability and vigorous rate response. In a very recent research study, Zhou et al.[39] deployed 3 Å zeolite molecular sieves within a PVDF matrix to cage residual DMF, steering $Li^+$ solvation toward an anion-dominated sheath. This strategy suppresses parasitic reactions, ensuring exceptional cycling stability. Concomitantly, the markedly enhanced $Li^+$ transference number and significantly reduced activation energy substantially improve rate capability. Such solvation modulation synchronizes robust interfaces with accelerated ion transport. Advancing beyond solvation control, multicomponent synergy enables enhanced performance through hierarchical ion/interface modulation. Wu et al.[40] incorporated UPyMA self-assembly nanofibers and LATP fillers into composite quasi-solid electrolytes (SL-CQSEs), enabling competitive anion anchoring and hydrogen bonding modulation. This synergy markedly improves cycling stability and rate capability. Anion anchoring elevates the $Li^+$ transference number and promotes a $Li_3N$/LiF-rich solid electrolyte interphase (SEI), enabling uniform Li deposition. The strategy simultaneously ensures fire safety and high-rate performance. Despite these advances, prevailing filler strategies remain constrained by suboptimal rate capability under practical conditions and insufficient interfacial stability at high current densities. The persistent capacity decay beyond high-rate cycling and ionic conductivity below $10^{-3}$ S $cm^{-1}$ in most systems fall short of industrial requirements for scalable SSBs, necessitating fundamentally redesigned coordination environments.

Among the plethora of potential fillers, the zirconium-based MOFs, with their superior chemical stability, present multiple advantages as fillers for CPEs. Specifically, among the large variety of Zr-based MOFs synthesized to date, MOF808 exhibits a highly ordered and chemically tunable mesoporous structure (pore diameter ∼4.8 Å) that can act as a liquid electrolyte reservoir.[41–43] In addition, a high density of acidic sites (Zr–OH/– $OH_2$ groups on the $Zr_6O_8$ clusters) of MOF808 is also an important aspect to consider.[44] Finally, the particle size and morphology of MOF808 can be readily controlled at the nanoscale to regulate the mesoporous and macroporous structure of the polymer substrate in CPEs. In this work, we strategically integrate chemically stable LATP and MOF808 fillers within a PVDF–HFP matrix (denoted as PLM-3) to reconfigure solvation dynamics. By immobilizing residual DMF via MOF808 confinement—which thermodynamically displaces solvent molecules with anions in the solvation sheath to form an anion-rich coordination architecture—this synergistic design significantly boosts $Li^+$ transport kinetics, thereby endowing the electrolyte with remarkable rate performance. Such anion-rich coordination not only facilitates rapid $Li^+$ desolvation—reducing the energy barrier by 15.8% ($-5.29$ vs $-6.28$ eV)—but concurrently establishes continuous ion-transport pathways, yielding a high $Li^+$ transference number (0.566) and enhanced ionic conductivity ($2.7 \times 10^{-4}$ S $cm^{-1}$). Crucially, the anion-enriched coordination accelerates interfacial charge transfer kinetics, enabling exceptional rate capability in Li‖PLM-3‖SC-NCM83 cells—delivering 219.5 mAh $g^{-1}$ at 0.1C and retaining 182.8 mAh $g^{-1}$ at 5C (4.3 V cutoff). This paradigm redefines the rate ceiling of polymer-based SSBs through targeted anion coordination chemistry.

## Results and discussion

### Preparation of polymer electrolytes and mechanism analysis

PVDF–HFP-based solid electrolytes containing varying concentrations of MOF808 fillers (0, 1, 3, and 5 wt%, labeled as PL, PLM-1, PLM-3, and PLM-5, respectively) (Fig. S1) were initially evaluated in SC-NCM83/CPEs/Li cells to assess the enhancement of long-term cycling stability and optimization of the diffusion coefficient (Fig. S2 and S3). These results indicate that 3 wt% MOF808 achieves an optimal balance between facilitating $Li^+$ transport and maintaining mechanical integrity. At lower loadings (e.g., 1 wt%), the amount of MOF808 is insufficient to remodel the solvation sheath or establish continuous ion-conducting pathways. Excess filler (e.g., 5 wt%), however, promotes agglomeration, disrupting polymer matrix integrity and ion transport, thereby compromising electrochemical performance. Consequently, subsequent detailed investigations were conducted on the PLM-3 electrolyte.

To investigate the interaction and solvation structure in both SSEs, we performed Fourier-transform infrared (FTIR) spectroscopy (Fig. 1a). The γ-phase PVDF peak (833 $cm^{-1}$) shifts to 840 $cm^{-1}$ (in PL) and 848 $cm^{-1}$ (in PLM-3), confirming enhanced β-phase formation.[45–47] This transition—driven by filler/– $CH_2$– interactions that promote a low to high polarity conversion[46]— yields the polar β-phase with a maximized dielectric constant, thereby enabling superior Li-salt dissociation and $Li^+$ transport. FTIR analysis reveals filler-induced shifts in characteristic bands: the – $CF_2$ symmetric stretching peak (1171 $cm^{-1}$) shifts to 1167/ 1169 $cm^{-1}$ upon filler incorporation (Fig. S4a), evidencing strong polymer–filler interactions.[48] Concurrently emerging – $SO_2$– asymmetric peaks (1371 $cm^{-1}$ for PLM-3; 1369 $cm^{-1}$ for PL; Fig. S4b) originate from MOF808-TFSI$^-$ interactions, which further enhance $Li^+$ dissociation and increase carrier
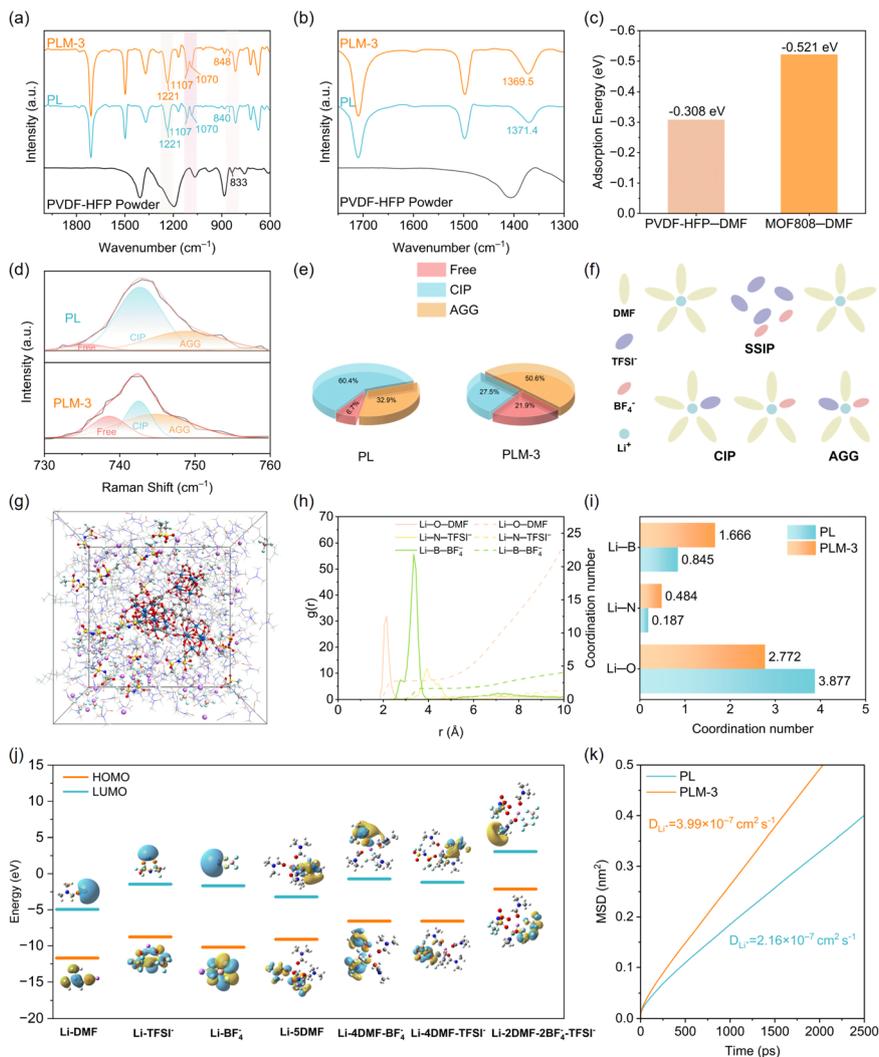
Fig. 1 (a) FT-IR spectra of PVDF−HFP powder, PL and PLM-3 electrolytes. (b) Locally enlarged image of (a). (c) DFT results for adsorption energies. (d) Raman spectra of PL and PLM-3 electrolytes. (e) The percentage of the corresponding solvation configuration. (f) Schematic diagram of the solvation structure. (g) MD simulation snapshots of PLM-3 electrolyte. (h) The radial distribution functions (g(r)) and coordination number (CN) of PLM-3 electrolyte. The solid lines represent g(r) and the dashed lines represent CN. (i) Coordination number of Li with B, N and O atoms in PL and PLM-3. (j) The LUMO and HOMO energy values of the different solvation structures. (k) MSD of Li$^+$ in PL and PLM-3 electrolytes.

concentration, thereby boosting ionic conduction.[49,50] The characteristic peaks at 673 cm$^{-1}$ for both PL and PLM-3 are attributed to DMF molecules bound to Li$^+$, while the absence of a peak at 658 cm$^{-1}$ confirms that no free DMF is present (Fig. S5).[45,51,52] The –CH$_3$ stretching vibration of DMF solvent (1371.4 cm$^{-1}$)[51] shifts to 1369.5 cm$^{-1}$ upon MOF808 incorporation (Fig. 1b), indicating robust coordination between MOF808 and DMF. Notably, PLM-3 exhibits enhanced DMF characteristic peak intensities relative to the PL electrolyte (Fig. S6), suggesting weaker Li$^+$–DMF coordination within PLM-3.[53] The adsorption energy calculated using density functional theory (DFT) further verified the strong adsorption effect of MOF808 on DMF molecules (Fig. 1c). The adsorption energy of DMF molecules on MOF808 is −0.521 eV, which is almost 2 times higher than that on PVDF−HFP chains (−0.308 eV; Fig. S7).

Raman spectroscopy was used to probe TFSI$^-$ coordination states (Fig. 1d–f). Peaks at 737–740 cm$^{-1}$, 743 cm$^{-1}$ and 746–

750 cm$^{-1}$ correspond to free anions (SSIP), Li$^+$–anion pairs (CIP), and aggregates (AGG), respectively.[54] The PL electrolyte exhibited 6.7% SSIP, 60.4% CIP, and 32.9% AGG (Fig. 1e). In PLM-3, CIP decreased with AGG surging to 50.6%, indicating enhanced Li$^+$–anion interactions. This shift does not reflect suppressed salt dissociation; rather, it signifies a reorganization of the solvation structure where MOF808-mediated DMF confinement promotes anion participation without compromising Li$^+$ availability. Molecular dynamics (MD) simulations were performed to elucidate the distinct role of MOF808 in modulating electrolyte solvation structures and the kinetic behavior of Li$^+$ transport. Fig. 1g and S8a present representative MD snapshots of the PL and PLM-3 electrolytes, respectively. The calculated mean square displacements (MSDs) of Li$^+$ in these electrolytes are presented in Fig. 1k. PLM-3 exhibits a steeper MSD slope compared to PL. The corresponding diffusion coefficients ($D_{Li}^+$) are $3.99 \times 10^{-7}$ cm$^2$ s$^{-1}$ for PLM-3

and $2.16 \times 10^{-7}$ cm$^2$ s$^{-1}$ for PL. Corresponding radial distribution functions (RDFs) and coordination numbers (CNs) for Li$^+$ interactions (DMF: Li–O; BF$_4^-$: Li–B; TFSI$^-$: Li–N) are detailed in Fig. 1h and S8b. Analysis reveals a significant enhancement in Li$^+$–BF$_4^-$ and Li$^+$–TFSI$^-$ coordination within PLM-3, evidenced by intensified RDF peaks and increased CNs (Li–B: 1.666; Li–N: 0.484) relative to the bulk PL electrolyte (Li–B: 0.845; Li–N: 0.187). Conversely, MOF808 incorporation markedly reduces DMF participation in the Li$^+$ solvation shell, as indicated by a decreased Li–O (DMF) CN of 2.772 in PLM-3 compared to 3.877 in bulk PL (Fig. 1i). Based on the simulation results, introducing MOF808 promotes Li salt anion participation in the solvation structure while displacing DMF molecules. The seemingly high AGG proportion (50.6%) in PLM-3 could be misconstrued as impairing ion transport, given that high AGG levels typically hinder Li$^+$ mobility.[55] However, in our designed system, this reflects a reconfigured solvation structure, where MOF808 sequesters DMF and promotes anion-coordinated contact ion pairs. These may exhibit a lower Li$^+$ dissociation barrier than solvent-bridged AGG, facilitating enhanced interfacial kinetics.[56] To further probe solvation effects, we quantitatively assessed desolvation energies across electrolyte configurations. The Li$^+$ desolvation energy in PL electrolyte (6.28 eV) exceeds that in PLM-3 (5.29 eV; Fig. S9), indicating distinct solvation behavior. Moreover, the confinement of DMF by MOF808 and the resultant solvation restructuring are pivotal to the enhanced electrochemical stability. The strong adsorption of DMF effectively removes solvent molecules from the electrolyte bulk, reducing their accessibility at the electrode interfaces. This suppression of solvent-dominated Li$^+$ solvation minimizes parasitic reduction/oxidation of DMF at the anode and cathode, respectively. Concurrently, the increased anion participation in the solvation sheath promotes the formation of a robust, inorganic-rich SEI and CEI, which further stabilizes the interfaces against degradation during high-rate cycling. Complementary DFT calculations reveal elevated lowest unoccupied molecular orbital (LUMO) and highest occupied molecular orbital (HOMO) energy levels (Fig. 1j): the increased LUMO enhances Li metal compatibility, while HOMO localization on BF$_4^-$ (vs. DMF) favors anion-derived cathode electrolyte interphase (CEI) formation. These complementary computational analyses reveal both the electronic structure and ionic transport dynamics in the electrolyte system. Thus, the high AGG content herein is a manifestation of a kinetically favorable, anion-dominated coordination environment, which concurrently enhances the Li$^+$ transference number and facilitates the formation of a robust inorganic-rich interphase, collectively contributing to the superior rate capability and enhanced electrochemical stability.

## The characterization of polymer electrolytes

Fig. S10 displays the X-ray diffraction (XRD) patterns of the prepared electrolyte membranes. Similar to PVDF-HFP, both PL and PLM-3 exhibit a broad characteristic polymer peak. Surface scanning electron microscopy (SEM) imaging (Fig. 2b and S13b) reveals a granular morphology for PLM-3, contrasting with the

dense, smooth texture of the PL electrolyte. The PL membrane is thinner (approximately 10.8 μm) than its PLM-3 counterpart, as shown in Fig. 2a and S13a. Energy dispersive spectroscopy (EDS) mapping (Fig. 2c and S13c) confirms the uniform dispersion of MOF808 throughout the PVDF–HFP matrix, attributable to their favorable compatibility. The ionic conductivities of the PL and PLM-3 electrolytes at different temperatures were measured (Fig. S11). Fig. 2d reveals that the PLM-3 electrolyte (2.61 $\times$ 10$^{-4}$ S cm$^{-1}$) surpasses its PL counterpart (1.97 $\times 10^{-4}$ S cm$^{-1}$) at room temperature, with error bars representing the standard deviation across multiple independent measurements(Fig. S12a). This enhancement correlates with a reduced ion migration activation energy (0.153 eV vs. 0.189 eV for PL), facilitated by incorporating 3 wt% MOF808 (Fig. S12b and c). Furthermore, the PLM-3 electrolyte exhibits a significantly enhanced Li$^+$ transference number (t$_{Li^+}$ = 0.566; Fig. 2e) relative to the PL electrolyte (t$_{Li^+}$ = 0.21; Fig. 2f). This elevated t$_{Li^+}$ arises from the synergistic effect of MOF808: its primary role in immobilizing DMF molecules to reconfigure the solvation sheath, coupled with its secondary interaction with TFSI$^-$ anions. This dual action collectively reduces anion mobility and promotes a Li$^+$ conductive pathway. Moreover, as evidenced by molecular dynamics simulations (Fig. 1h and i), the filler-induced attenuation of Li$^+$–DMF coordination concomitantly enhances Li$^+$–anion interactions. Such preferential anion coordination establishes continuous conduction pathways while suppressing detrimental anion polarization—a critical kinetic bottleneck that traditionally constrains rate capability in polymer electrolytes. Consequently, the restructured ion transport network synergistically reduces the desolvation energy barrier for Li$^+$, thereby enabling high-rate performance in SSBs. Direct current polarization measurements revealed a lower electronic conductivity for the PLM-3 electrolyte (3.91 $\times$ 10$^{-11}$ S cm$^{-1}$) compared to the PL electrolyte (1.17 $\times$ 10$^{-10}$ S cm$^{-1}$), indicative of its superior insulating properties (Fig. 2g). Fig. 2h demonstrates that PLM-3 exhibits the highest tensile strength (5.82 MPa), surpassing that of PL (5.35 MPa) and PVDF-HFP (5.15 MPa). The characteristic tensile curve features an initial plateau followed by an abrupt drop. This behavior arises from macromolecular chain alignment under tension, enhancing electrolyte toughness.[57,58] It is generally recognized that the addition of organic components can reduce electrolyte stiffness.[59] As predicted, the tensile strength of PLM-3 is higher than that of PL (Fig. S14), but the elongation at break is reduced. In summary, achieving ideal mechanical properties requires selecting an appropriate ratio of inorganic to organic components. Thermogravimetric analysis (TGA) indicates comparable residual DMF content (Fig. S15), suggesting that the conductivity improvement in PLM-3 is not attributable to variations in bulk DMF retention. Instead, the improvement stems primarily from the MOF808-induced remodeling of the local solvation structure, which facilitates anion participation in Li$^+$ coordination and enhances carrier mobility, as elucidated by our spectroscopic and computational analyses. Benefiting from the confinement of DMF molecules and the modulated solvation structure, the ESW of the PLM-3 electrolyte is broadened. Linear sweep voltammetry (LSV) analysis confirms an expanded ESW
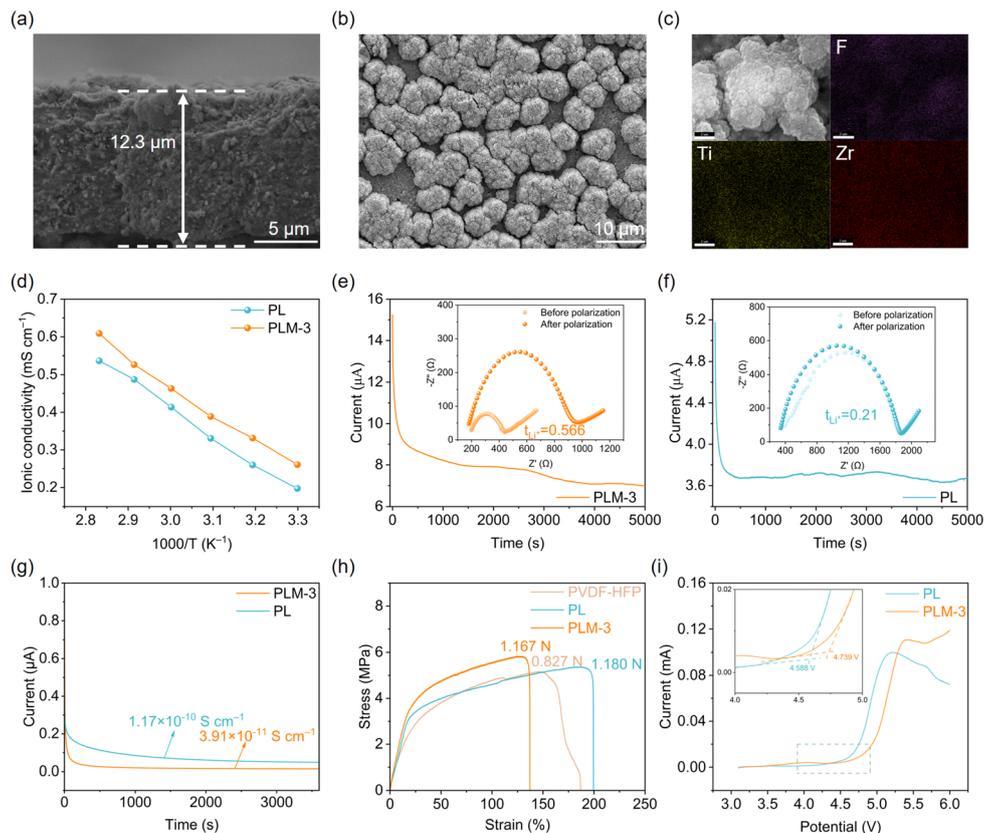
**Fig. 2** (a) Cross-sectional and (b) surface SEM images of PLM-3 electrolyte. (c) Surface energy dispersive spectroscopy (EDS) maps of F, Ti and Zr elements in the PLM-3 electrolyte. (d) Ionic conductivities of different samples at different temperatures. Chronoamperometry profiles and AC impedance spectra before and after polarization (inset) of (e) Li/PLM-3/Li and (f) Li/PL/Li cells. (g) Current–time curves of PL and PLM-3 electrolytes at polarization voltage of 0.5 V. (h) Stress–strain curves of PVDF–HFP, PL and PLM-3 electrolytes. (i) Electrochemical stability window of CPEs.

from 4.588 V to 4.739 V (Fig. 2i), highlighting its considerable potential for application with high voltage cathodes.

### Li plating/stripping behavior and post analysis

Coulombic efficiency (CE) measurements, conducted in Li‖Cu cells at 0.2 mA cm$^{-2}$, assessed Li plating/stripping reversibility. The modified Aurbach CE method revealed superior stability for the Li metal anode with PLM-3 electrolyte, yielding a significantly higher initial CE (94.2%) compared to PL electrolyte (92.2%) (Fig. 3a). While the PL electrolyte cell exhibited rapid CE decay and failed at the 52nd cycle, the PLM-3 cell maintained an average CE of 93.5% for over 200 cycles (Fig. 3b). Tafel and constant-current charge/discharge (CCD) analyses of Li symmetric cells further evaluated the impact of CPEs on Li reaction kinetics and interfacial stability (Fig. S19a). PLM-3 exhibits a significantly higher exchange current density (0.251 mA cm$^{-2}$) than PL (0.151 mA cm$^{-2}$), signifying drastically reduced charge transfer barriers (Fig. 3c). Complementary Tafel analysis and constant-current stripping/plating profiles corroborated markedly accelerated Li$^+$ reaction kinetics at the anode interface. This kinetic enhancement stems directly from the reconstructed anion-enriched solvation sheath, which lowers the Li$^+$ desolvation energy barrier by weakening Li$^+$–DMF coordination as evidenced by molecular dynamics simulations.

Critically, such optimized interfacial kinetics govern the evolution of Li deposition morphology toward uniformity. Corresponding SEM characterization distinctly reveals contrasting Li deposition patterns on copper current collectors in Li‖Cu cells: while the PL electrolyte yields loose, dendritic Li deposits (Fig. S16a), the PLM-3 electrolyte facilitates the formation of larger, densely packed Li particles, ultimately resulting in a smooth and continuous deposition layer (Fig. S16b). Notably, previous studies have demonstrated that the Li deposition morphology and the corresponding ion desolvation mechanism of SSBs heavily depend on the solvation structure.[60] Temperature-dependent electrochemical impedance tests (EIS) of fresh Li‖Li symmetric cells (Fig. S17a and S17b) further quantified the desolvation energy ($E_{des}$), representing the activation barrier for Li$^+$ desolvation at the SEI/electrolyte interface.[61] Cells employing PLM-3 electrolyte consistently exhibited lower impedance than those with PL electrolyte. Crucially, $E_{des}$ for PLM-3 (16.73 kJ mol$^{-1}$) was 11.2% lower than for PL (18.85 kJ mol$^{-1}$). Corresponding fitting analyses (Fig. S17c) confirm that PLM-3 minimizes the activation energy for charge transfer, facilitating Li$^+$ participation in electrode reactions. This reduction correlates with attenuated Li$^+$–DMF coordination in PLM-3, lowering the desolvation energy barrier and thereby promoting uniform Li deposition.
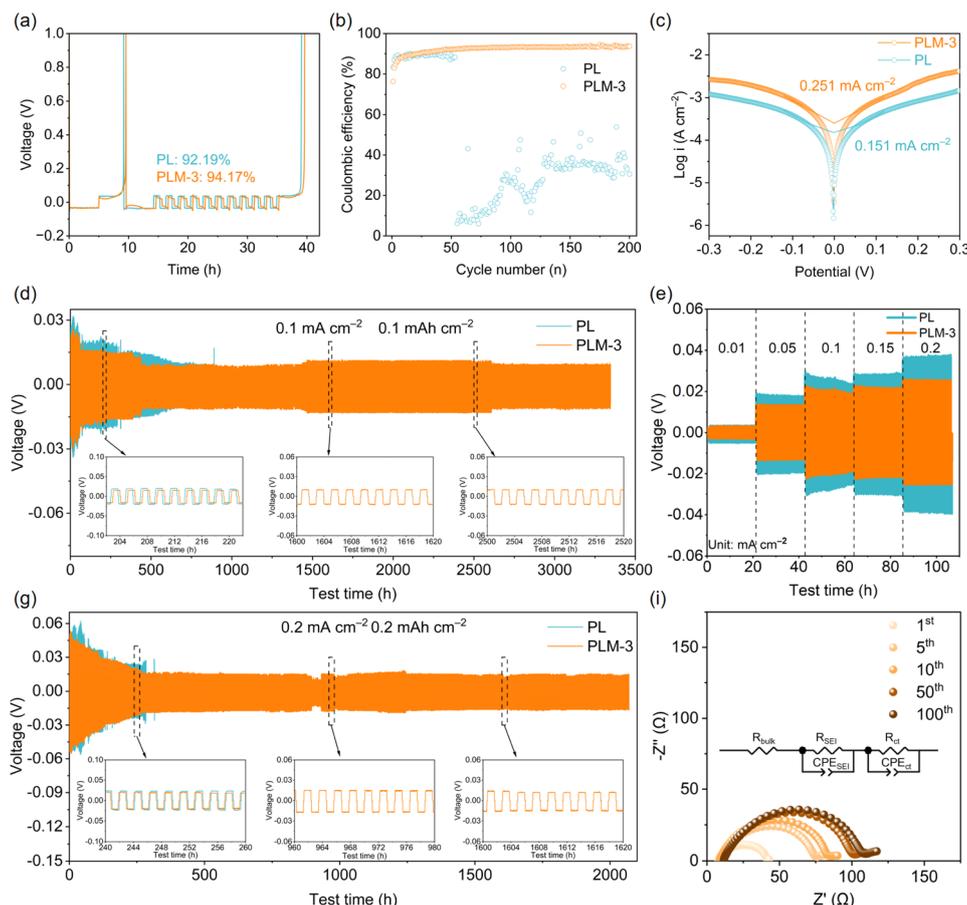
**Fig. 3** (a) Modified Aurbach CE test in Li‖Cu cells with PL and PLM-3. (b) Li plating/stripping CEs in Li‖Cu cells with PL and PLM-3 with 0.1 mA cm$^{-2}$ and 0.1 mAh cm$^{-2}$. (c) Tafel plots obtained from Li symmetric cells using PL and PLM-3. (d) Galvanostatic charge/discharge performance of Li/CPEs/Li symmetric cells with PL and PLM-3 at a current density of 0.1 mA cm$^{-2}$. (e) Rate performance of Li/CPEs/Li symmetric cells with PL and PLM-3 electrolytes. (f) Galvanostatic charge/discharge performance of Li/CPEs/Li symmetric cells with PL and PLM-3 at a current density of 0.2 mA cm$^{-2}$. (g) Nyquist plots of Li/PLM-3/Li symmetric cells after 100 cycles.

Beyond interfacial structural stability, the chemical composition of the SEI formed on cycled Li metal anodes critically governs interfacial electrochemical kinetics and stability. Accordingly, X-ray photoelectron spectroscopy (XPS) profiling was utilized to probe the SEI's surface species (Fig. S18). The N 1s and F 1s spectra for both PL and PLM-3 electrolytes reveal N$^-$ and F$^-$ containing species within the SEI, originating from LiTFSI and LiBF$_4$ decomposition. XPS analysis of both cycled anodes reveals characteristic C 1s peaks at ~284.8 eV (C–C/C–H), ~286.7 eV (C–O), ~288.3 eV (C=O) and ~290.2 eV (CO$_3^{2-}$), with an additional C–N signal at ~286.4 eV.[62] The absence of C–F signatures confirms polymer matrix retention, demonstrating superior interfacial compatibility between CPEs and Li metal anodes. The N 1s spectra exhibit Li$_3$N (~398.5 eV) and N–C=O (~399.9 eV) components, the latter indicating amide group participation in SEI formation. Comparative analysis with solvation structures (Fig. 1e) and energy levels (Fig. 1j) establishes that PLM-3-derived SEI layers show significantly intensified Li$_3$N and N–C=O peaks vs. PL-derived counterparts, attributable to enhanced LiTFSI decomposition. Concurrently, F 1s spectra revealed an inorganic-rich SEI dominated by LiF, with elevated LiF content in PLM-3 vs. PL electrolytes, indicating enhanced Li$^+$ salt dissociation. This LiF

enrichment promotes uniform Li deposition and suppresses dendritic growth.[63,64] In addition, for the PLM-3 electrolyte, a pronounced Zr 3d doublet emerges at 181–189 eV, whereas no discernible Zr 3d signal is detected for PL, confirming that the Zr-containing inorganic species originate from the MOF808 fillers at the Li/CPE interface.[65] Deconvolution of the Zr 3d region shows a dominant doublet with the Zr 3d$_{5/2}$ component centered near ~182.5 eV, characteristic of Zr$^{4+}$ in Zr–O coordination environments such as ZrO$_2$-like or lithium zirconate-type phases.[66,67] Considering that MOF808 is constructed from hydroxo/aquo-terminated Zr$_6$O$_8$ clusters linked by benzene-1,3,5-tricarboxylate ligands,[68] these features indicate that partial ligand loss and structural rearrangement of the Zr$_6$O$_8$ nodes at the highly reducing Li surface give rise to Zr–O–rich inorganic domains embedded within the SEI. Such Zr–O–rich interphases have been reported to serve as mechanically robust and ionically conductive scaffolds that suppress parasitic electrolyte decomposition and homogenize Li$^+$ flux,[69,70] which is consistent with the smoother Li deposition morphology and enhanced interfacial stability observed for Li anodes cycled in PLM-3. Collectively, these XPS analyses demonstrate MOF808's capacity to immobilize TFSI$^-$ anions and DMF molecules, thereby weakening Li$^+$–O binding in

the $[\mathrm{Li(DMF)}_x]^+$ solvation structure. This mechanism inhibits interfacial DMF decomposition and stabilizes SEI formation. Consequently, incorporating MOF808 fillers improves the electrochemical stability of PVDF–HFP-based solid electrolytes against Li metal, thus establishing the robust interfacial integrity essential for sustaining rapid charge–discharge capability during high-rate operation. The Li/PLM-3/Li symmetric cell exhibits reduced polarization during cycling across various current densities (Fig. 3e and S19b). It maintains stable operation for over 3200 h at 0.1 mA cm$^{-2}$/0.1 mAh cm$^{-2}$ with minimal voltage hysteresis, contrasting sharply with the Li/PL/Li cell, where polarization escalates abruptly after 890 hours (Fig. 3d). Voltage profiles at 0.2 mA cm$^{-2}$/0.2 mAh cm$^{-2}$ further demonstrate PLM-3's superior stability, achieving more than 2000 h of smooth, symmetrical stripping/plating without short-circuiting (Fig. 3f). Even under demanding conditions (0.25 mA cm$^{-2}$/0.5 mAh cm$^{-2}$), PLM-3 sustains cycling for over 1200 h—surpassing PL's 480 h lifespan (Fig. S20). At 0.5 mA cm$^{-2}$/0.5 mAh cm$^{-2}$, PLM-3 delivers 350 hours of stable operation, while PL fails beyond 150 hours due to accelerated interfacial side reactions (Fig. S21). Quasi-*operando* EIS corroborates enhanced interfacial stability, with Li/PLM-3/Li consistently exhibiting lower post-cycling resistance than Li/PL/Li (Fig. 3g and S22). This exceptional interfacial durability, arising directly from the anion-enriched solvation structure engineered by MOF808, ultimately underpins the rate capability demonstrated in high voltage full cells. Collectively, these results confirm that MOF808 incorporation mitigates Li–electrolyte side reactions and interfacial degradation.

## Electrochemical performance of polymer electrolytes

The initial charge–discharge voltage profiles of SC-NCM83 tested in PL and PLM-3 electrolytes are illustrated in Fig. 4a. Notably, at 0.1C, SC-NCM83/PLM-3/Li cells demonstrate a superior discharge specific capacity (219.5 mAh g$^{-1}$), effectively utilizing a greater amount of recyclable active Li$^+$. The long-term cycling performances of the SC-NCM83/PL/Li and SC-NCM83/PLM-3/Li cells at various rates are also examined. At a rate of 1C, the SC-NCM83/PLM-3/Li cell can be stably operated for more than 200 cycles, and the capacity retention after 200 cycles reaches up to 93.73%, with a high average coulombic efficiency of 99.5%. In contrast, the SC-NCM83/PL/Li cell can stably cycle for 200 cycles, and then it rapidly decays. The capacity retention with PL electrolyte after 200 cycles is only 81.83% (Fig. 4b and c). Even at small rates of 0.33C and 0.5C, which accentuate the instability at high voltage, the SC-NCM83/PLM-3/Li cells still exhibit significantly better cycling stability (Fig. S23 and S24), while the discharge specific capacity of the SC-NCM83/PL/Li cells declines rapidly. Additionally, to substantiate the thermal stability, extended cycle tests were executed at 45 °C (Fig. 4e). The significantly improved cycling performance of the SC-NCM83/PLM-3/Li cell at 45 °C underscores its exceptional interfacial thermal resilience. MOF808 enhances high-temperature performance by sequestering DMF to suppress solvent decomposition and by fostering a thermally stable, anion-rich interphase (LiF/Li$_3$N/Zr–O). This dual stabilization mechanism mitigates interfacial degradation and preserves electrode integrity under thermal stress. The specific capacities of the SC-

NCM83/PLM-3/Li cell at 0.1, 0.2, 0.5, 1, 2 and 5C are 219.5, 212.1, 203.7, 197.0, 191.7 and 182.8 mAh g$^{-1}$, respectively (Fig. 4d and S25). Notably, the cell maintains an exceptional capacity retention of 83.3% at 5C, representing a critical advancement in rate capability for high voltage polymer-based SSBs. This enhancement stems directly from the anion-tailored solvation structure, which effectively minimizes kinetic barriers. The PLM-3 electrolyte outperforms the SC-NCM83/PL/Li system significantly, owing to its superior ionic conductivity and Li$^+$ transference number. Remarkably, when the rate is reset to 0.1C, the specific capacity recovers to 214.2 mAh g$^{-1}$, demonstrating exceptional electrochemical reversibility. Further mechanistic analysis reveals that the optimized rate performance originates from accelerated intermolecular transport kinetics, attributed to weakened Li$^+$–DMF coordination that reduces the Li$^+$ desolvation energy barrier. To the best of our knowledge, as depicted in Fig. 4f, this study employing the PLM-3 electrolyte has outperformed several previously published studies. At last, to verify the safety of the PLM-3 electrolyte, a flame retardancy test was conducted. As shown in Fig. S26, the PLM-3 electrolyte ceased to burn within 5 s of flame exposure, indicating its potential for use in highly safe Li metal batteries.

## The characterization of the CEI interphase and its construction mechanism

To elucidate the mechanisms underlying performance enhancement, we analyzed the structure and surface composition of SC-NCM83 cathodes post-cycling. Structural instability constitutes a major factor driving progressive capacity fading, necessitating detailed investigation of cathode degradation. XRD analysis was conducted to track crystallographic evolution. The pristine SC-NCM83 exhibited a high $I_{(003)}/I_{(104)}$ intensity ratio (2.68), signifying well-ordered layering with minimal Li/Ni cation mixing (Fig. S27a). After 100 cycles, SC-NCM83 in PLM-3 electrolyte retained a higher $I_{(003)}/I_{(104)}$ ratio (2.46) than in PL electrolyte (2.28), indicating reduced cation mixing with CPEs.[80] This enhanced structural preservation using PLM-3 electrolyte stems from effective mitigation of continuous detrimental electrolyte SC-NCM83 reactions during charge/discharge cycles—reactions prominently driving reconstruction in PLM-3 electrolyte. In PLM-3 electrolyte, SC-NCM83 exhibits a markedly suppressed H2 to H3 phase transition of the (003) peak, demonstrating a minimal angular shift of merely 0.02°. This contrasts sharply with the pronounced peak migration observed in PL electrolyte. Synergistic stabilization is evidenced by analogous trends in the (102) and (104) diffraction planes. Post 100-cycle XRD analysis further reveals significant low-angle migration of the (003) peak in PL-based SC-NCM83 (Fig. S27b), attributable to irreversible Li$^+$ loss and enhanced oxygen interlayer repulsion. SEM of both cycled electrodes (Fig. 5a and b) confirmed the structural integrity of the single-crystal morphology. Polycrystalline secondary particles cycled in PL electrolyte developed substantial cracking and delamination after 100 cycles. In contrast, SC-NCM83 particles in PLM-3 electrolyte retained an intact single-crystal architecture, attributable to a conformal CEI layer that mechanically stabilizes the cathode and suppresses micro-crack propagation during cycling.[81] The surface structure of SC-NCM83 particles was
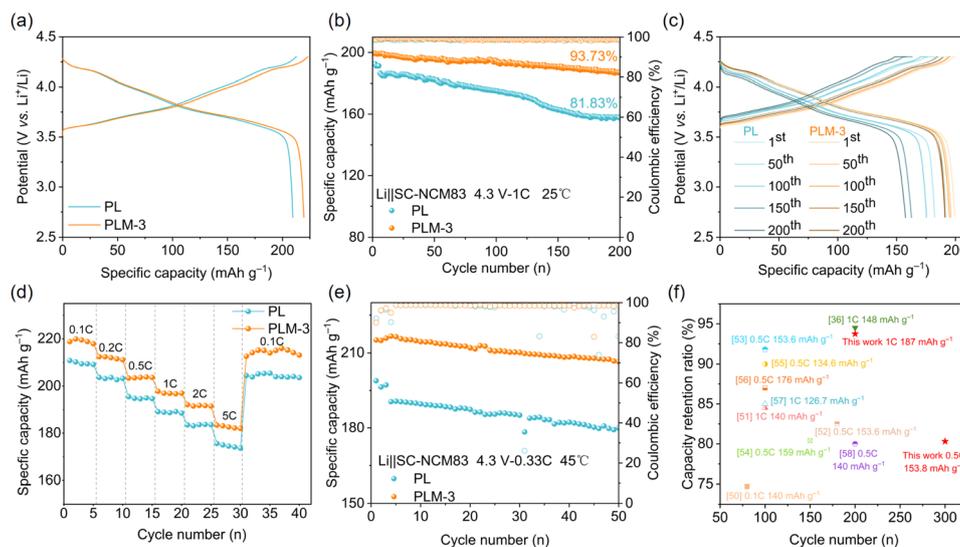
**Fig. 4** (a) Initial charge and discharge curves of SC–NCM83/CPEs/Li cells at 0.1C and 25 °C between 2.7 and 4.3 V. (b) Rate performance of SC–NCM83/CPEs/Li cells between 2.7 and 4.3 V. (c) Cycling performance of SC–NCM83/CPEs/Li cells at 0.33C and 45 °C between 2.7 and 4.3 V. (d) Cycling performance of SC–NCM83/CPEs/Li cells at 1C and 25 °C between 2.7 and 4.3 V. (e) Charge and discharge curves of SC–NCM83/CPEs/Li cells at 1C and 25 °C between 2.7 and 4.3 V. (f) 3D comparison of the electrochemical performances of our work with recently reported high voltage cathode materials in polymer–based Li metal batteries.[48,71–79]

further characterized by Transmission Electron Microscopy (TEM). The TEM images show that a uniform CEI with a thickness of ~3 nm formed on the surface of the SC-NCM83 particles cycled with the PLM-3 electrolyte, while an uneven CEI of ~12.17 nm was observed for those using the PL electrolyte (Fig. 5c and d). Critically, this order-of-magnitude reduction in CEI thickness—a direct consequence of the anion-enriched solvation structure—minimizes interfacial ion-transfer resistance and underpins the exceptional rate capability. Fig. 5e presents the CEI compositions for both electrolytes, revealing comparable C 1s spectral features for the cycled cathodes. The detection of a distinct peak at ~398 eV in the N 1s spectrum of PLM-3 electrolyte, attributable to $Li_3N$, indicates a hybrid organic/inorganic CEI. Crucially, the presence of the anti-oxidative N–C=O moiety significantly enhances long-term cycling stability by mitigating electrolyte decomposition and suppressing cathode surface degradation.[82] XPS analysis of PLM-3-cycled SC-NCM83 cathodes exhibits reduced organic decomposition products relative to conventional PL electrolytes, attributed to suppressed DMF decomposition. This attenuation signifies a robust anion-derived CEI capable of inhibiting further oxidative electrolyte decomposition. Spectral evidence of persistent metal–oxygen signatures in the O 1s spectrum further corroborates the formation of a thinner CEI. This ultrathin and inorganic-rich interphase synergistically facilitates rapid $Li^+$ desolvation kinetics and charge transfer at the cathode interface, ultimately enabling the exceptional high-rate capability demonstrated in full cells. In general, the robust interaction between MOF808 and DMF solvent weakens $Li^+$–DMF coordination, thereby increasing anion participation in the solvation sheath and suppressing DMF decomposition at high voltage cathode interfaces. This process facilitates the formation of a thin,

compact, anion-derived CEI, which mitigates structural decay in SC-NCM83 particles and enhances cycling stability.

Furthermore, the activation energy ($E_{ct}$) for $Li^+$ desolvation was calculated from Arrhenius analysis of temperature-dependent EIS (30–60 °C) in Li‖SC-NCM83 cells (Fig. S28a and S28b). The $E_{ct}$ value in PLM-3 electrolyte (37.93 kJ mol$^{-1}$) is lower than that in PL electrolyte (40.98 kJ mol$^{-1}$) (Fig. S28c). These results collectively demonstrate that $Li^+$–DMF coordination in PLM-3 reduces the desolvation energy barrier, thereby facilitating accelerated $Li^+$ transport and desolvation kinetics. Additionally, the Li‖PLM-3‖SC-NCM83 cell exhibits a lower activation energy ($E_{CEI}$) for $Li^+$ diffusion through the CEI layer (23.92 kJ mol$^{-1}$) (Fig. S28d) than that for Li‖PL‖SC-NCM83 cell (26.61 kJ mol$^{-1}$). Critically, this concerted lowering of activation barriers for both interfacial desolvation and CEI permeation directly underpins the exceptional high-rate capability. The electrochemical stability of SSBs is intimately linked to interfacial structural evolution. To probe interfacial compatibility, we assessed the variation in interfacial resistance for Li‖PL‖SC-NCM83 and Li‖PLM-3‖SC-NCM83 cells before and after cycling using EIS (Fig. S29). The interfacial resistance of the Li‖PL‖SC-NCM83 cell persistently exceeded that of its Li‖PLM-3‖SC-NCM83 counterpart, both pre-cycling and post-cycling. This disparity signifies accelerated interfacial reaction kinetics in the Li‖PLM-3‖SC-NCM83 cell, originating from facilitated $Li^+$ desolvation and transport at its electrodes. Furthermore, the significantly lower post-cycling interfacial resistance demonstrates superior interfacial compatibility, which directly enhances cycling stability.[83] The galvanostatic intermittent titration (GITT)-derived $Li^+$ diffusion coefficients for PLM-3 exceed those of PL (Fig. S30), evidencing both swifter ion transport and superior structural integrity. To assess the stability of SSBs employing high voltage cathodes, *in situ* EIS
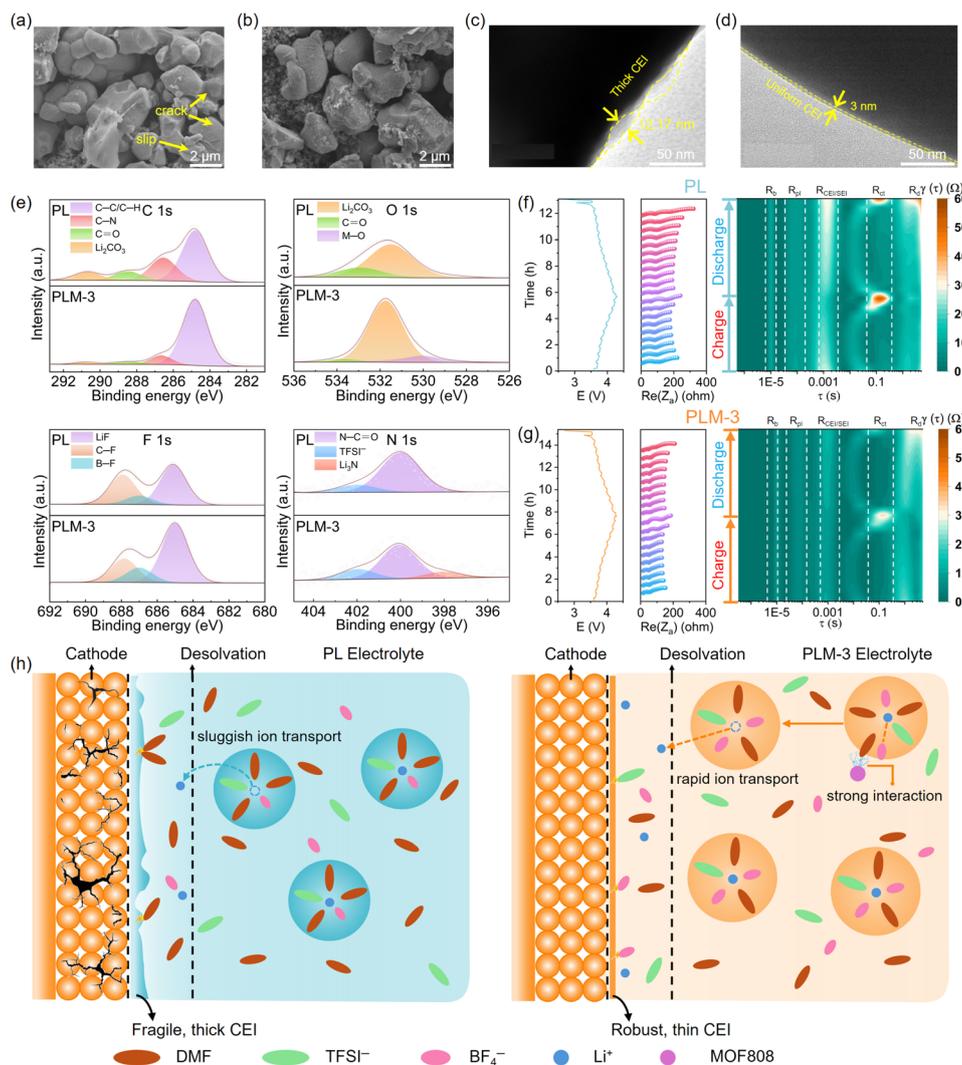
**Fig. 5** SEM images of 100-cycled SC-NCM83 cathodes in PL (a) and PLM-3 (b). TEM images of the CEI layers formed in PL (c) and PLM-3 (d). (e) XPS spectrum for C 1s, O 1s, F 1s and N 1s of the cycled SC-NCM83 cathode surface with PL and PLM-3 electrolytes. (f) Li‖PL‖SC-NCM83 charge–discharge curves and *in situ* EIS at 2.7–4.3 V and the corresponding DRT contour stacking plot. (g) Li‖PLM-3‖SC-NCM83 charge–discharge curves and *in situ* EIS at 2.7–4.3 V and the corresponding DRT contour stacking plot. (h) Schematic illustration of the solvation structure and the CEIs in the PL and PLM-3 electrolytes.

coupled with distribution of relaxation times (DRT) analysis was performed throughout cycling. Frequency-to-time domain transformation of Nyquist plots yielded enhanced temporal resolution of impedance evolution during charge/discharge cycles (Fig. 5f and g). Impedance and DRT analyses deciphered voltage-dependent Li$^+$ migration and conversion dynamics for both cell configurations. The peaks at $\sim10^{-5}$ s, $\sim10^{-3}$ s, $\sim10^{-1}$ s, and $\sim10$ s, represent the bulk resistance ($R_b$), SEI/CEI resistance ($R_{CEI/SEI}$), charge transfer resistance ($R_{ct}$), and diffusion resistance ($R_d$), respectively.[84–86] Particularly, the peak near $10^{-4}$ s is assigned to the polymer layer resistance ($R_{pl}$) on the surface of the cathode or anode.[87] Across an extended time domain ($10^{-6}$–$10^{-1}$ s), the Li‖PLM-3‖SC-NCM83 configuration exhibits significantly lower overall resistance compared to Li‖PL‖SC-NCM83 (Fig. 5f and g), indicating superior ion transport and conversion kinetics.[84–86] Analysis of the $R_{pl}$ reveals distinct behavior: within the PL system, $R_{pl}$ undergoes an initial

decrease followed by an increase during cycling, signifying progressive decomposition and irreversible structural alteration of the polymer layer. Conversely, the $R_{pl}$ magnitude and position in the PLM-3 system remain remarkably stable, demonstrating exceptional polymer-layer integrity under high voltage operation. Similarly, the $R_{CEI/SEI}$ in the PLM-3 system is markedly lower and exhibits minimal variation during cycling. This contrasts sharply with the unstable $R_{CEI/SEI}$ observed in the PL system and further confirms the enhanced interfacial stability afforded by the PLM-3 modification under high voltage conditions. Notably, this resistance hierarchy translates directly into the cell's unrivaled rate capability, underscoring that interfacial kinetic robustness rather than mere stability is the decisive enabler for high-power SSBs. This kinetic superiority is vividly illustrated in Fig. 5h, which contrasts the solvation architectures and interfacial chemistries of PL and PLM-3 electrolytes. PL electrolyte exhibits solvent-dominated Li$^+$ solvation shells

due to strong DMF–Li coordination, resulting in sluggish ion desolvation and heterogeneous organic-rich CEIs. In contrast, the PLM-3 electrolyte exploits MOF808's confinement to sequester DMF, reconfiguring the primary solvation shell into an anion-coordinated environment where anions replace solvent molecules in Li$^+$ coordination. This engineered solvation structure displaces solvent molecules with anions, markedly reducing the desolvation energy barrier while promoting inorganic-rich CEI formation. Crucially, concurrent optimization of bulk ion transport and interfacial kinetics underpins outstanding rate capability.

## Conclusions

In summary, we propose a novel strategy that modulates the solvation structure in PVDF–HFP-based SSEs by introducing MOF808 as a filler, overcoming the intrinsic rate limitations of polymer-based SSBs. The strong anchoring effect of MOF808 on DMF weakens its ability to participate in solvation, resulting in more anions participating in the solvation structure. This reconstructed coordination architecture reduces Li$^+$ desolvation energy by 15.8% (−5.29 vs. −6.28 eV) and elevates the Li$^+$ transference number to 0.566—kinetic enablers that directly unlock unprecedented rate capability. Consequently, Li‖PLM-3‖SC-NCM83 full cells deliver 182.8 mAh g$^{-2}$ at 5 C with 83.3% capacity retention. Crucially, the anion-enriched environment concurrently stabilizes interfaces: it fosters inorganic-rich SEI/CEI layers that suppress parasitic reactions, enabling 3200 h of dendrite-free cycling in Li symmetric cells and 93.73% capacity retention after 200 cycles at 1C (4.3 V cutoff). This work transcends conventional filler paradigms, eradicating the persistent solvent-residue dilemma in PVDF–HFP-based electrolytes while establishing solvation-structure engineering as a scalable lever to concomitantly unlock high-rate operation and interfacial robustness in SSBs.

## Author contributions

Z. W. contributed to conceptualization, formal analysis, and writing of the original draft. Z. H. contributed to formal analysis, and resources. H. G. contributed to data curation, and resources. T. H. contributed to formal analysis, and resources. J. G. contributed to formal analysis, and resources. J. L. contributed to formal analysis, and resources. N. F. contributed to formal analysis, and resources. Z. W. contributed to formal analysis, and methodology. X. Y. contributed to formal analysis, and methodology. Y. L. contributed to formal analysis, and methodology. J. L. contributed to project administration. Y. W. contributed to conceptualization, supervision, and writing (review and editing). Q. Z. contributed to formal analysis, and methodology. J. H. contributed to conceptualization, supervision, and writing (review and editing). X. R. contributed to conceptualization, supervision, and writing (review and editing).

## Conflicts of interest

The authors declare no conflict of interest.

## Data availability

The detailed experimental procedures, figures and tables are provided in the supplementary information (SI). The data supporting this article have been included as part of the supplementary information. Supplementary information is available. See DOI: https://doi.org/10.1039/d5sc07849k.

## Acknowledgements

## Notes and references

1 M. Armand and J.-M. Tarascon, *Nature*, 2008, **451**, 652–657.
2 T. Yuan, S. Luo, L. Soule, J.-H. Wang, Y. Wang, D. Sun, B. Zhao, W. Li, J. Yang, S. Zheng and M. Liu, *Mater. Today*, 2021, **45**, 8–19.
3 J. Zhang, H. Zhang, S. Weng, R. Li, D. Lu, T. Deng, S. Zhang, L. Lv, J. Qi, X. Xiao, L. Fan, S. Geng, F. Wang, L. Chen, M. Noked, X. Wang and X. Fan, *Nat. Commun.*, 2023, **14**, 2211.
4 E. Quartarone and P. Mustarelli, *Chem. Soc. Rev.*, 2011, **40**, 2525.
5 Y. Zhao, C. Wu, G. Peng, X. Chen, X. Yao, Y. Bai, F. Wu, S. Chen and X. Xu, *J. Power Sources*, 2016, **301**, 47–53.
6 Z. Chang, H. Yang, X. Zhu, P. He and H. Zhou, *Nat. Commun.*, 2022, **13**, 1510.
7 S. Kim, H. Oguchi, N. Toyama, T. Sato, S. Takagi, T. Otomo, D. Arunkumar, N. Kuwata, J. Kawamura and S.-i. Orimo, *Nat. Commun.*, 2019, **10**, 1081.
8 S. Kim, J.-S. Kim, L. Miara, Y. Wang, S.-K. Jung, S. Y. Park, Z. Song, H. Kim, M. Badding, J. Chang, V. Roev, G. Yoon, R. Kim, J.-H. Kim, K. Yoon, D. Im and K. Kang, *Nat. Commun.*, 2022, **13**, 1883.
9 Z. Li, R. Yu, S. Weng, Q. Zhang, X. Wang and X. Guo, *Nat. Commun.*, 2023, **14**, 482.
10 Y. Xia, P. Zhou, X. Kong, J. Tian, W. Zhang, S. Yan, W.-h. Hou, H.-Y. Zhou, H. Dong, X. Chen, P. Wang, Z. Xu, L. Wan, B. Wang and K. Liu, *Nat. Energy*, 2023, **8**, 934–945.
11 X. Zhan, M. Li, X. Zhao, Y. Wang, S. Li, W. Wang, J. Lin, Z.-A. Nan, J. Yan, Z. Sun, H. Liu, F. Wang, J. Wan, J. Liu, Q. Zhang and L. Zhang, *Nat. Commun.*, 2024, **15**, 1056.
12 B. Scrosati, *J. Appl. Electrochem.*, 1972, **2**, 231–238.
13 R. Liao, C. Li, M. Zhou, R. Liu, S. Liu and D. Wu, *Chem. Sci.*, 2024, **15**, 18327–18334.
14 M. Tayyab, L. Zizhe, S. Rauf, Z. Xu, R. U. R. Sagar, F. Faiz, Z. Tayyab, R. U. Rehman, M. Imran, A. Waheed, R. Javed, A. Surulinathan, Z. Zafar, X.-Z. Fu and J.-L. Luo, *Chem. Sci.*, 2025, **16**, 3362–3407.

15 Z. Sun, Q. Yin, H. Chen, M. Li, S. Zhou, S. Wen, J. Pan, Q. Zheng, B. Jiang, H. Liu, K. Kim, J. Li, X. Han, Y. B. He, L. Zhang, M. Li and Q. Zhang, *Interdiscip. Mater.*, 2023, **2**, 635–663.

16 W. Zha, W. Li, Y. Ruan, J. Wang and Z. Wen, *Energy Storage Mater.*, 2021, **36**, 171–178.

17 B. Jiang, Y. Wei, J. Wu, H. Cheng, L. Yuan, Z. Li, H. Xu and Y. Huang, *EnergyChem*, 2021, **3**, 100058.

18 X. Han, L. Gu, Z. Sun, M. Chen, Y. Zhang, L. Luo, M. Xu, S. Chen, H. Liu, J. Wan, Y.-B. He, J. Chen and Q. Zhang, *Energy Environ. Sci.*, 2023, **16**, 5395–5408.

19 J. Meng, M. Yin, K. Guo, X. Zhou and Z. Xue, *Nano-Micro Lett.*, 2025, **17**, 248.

20 H. Zhang, Y. Zhang, X. Du, X. Ge, Z. Yuan, S. Zhang, D. Wang, Z. Lv, X. Zhou, J. Zhang and G. Cui, *Adv. Mater.*, 2025, **37**, e07621.

21 T. Li, K. Chen, B. Yang, K. Li, B. Li, M. He, L. Yang, A. Hu and J. Long, *Chem. Sci.*, 2024, **15**, 12108–12117.

22 S. Wen, Z. Sun, X. Wu, S. Zhou, Q. Yin, H. Chen, J. Pan, Z. Zhang, Z. Zhuang, J. Wan, W. Zhou, D. L. Peng and Q. Zhang, *Adv. Funct. Mater.*, 2025, **35**, 2422147.

23 H. Wang, L. Qian, Y. Zheng, S. Duan, B. Qin, Z. Liu, Z. Li, Q. Ma, Y. Jiang, W. Yan and J. Zhang, *Adv. Mater.*, 2025, **37**, e10197.

24 A. Du, H. Lu, S. Liu, S. Chen, Z. Chen, W. Li, J. Song, Q. H. Yang and C. Yang, *Adv. Energy Mater.*, 2024, **14**, 2400808.

25 L. Dai, M. Cai, X. Zhou, W. Liang, Z. Zhao, Z. Xia, F. Huang, J. Jiang, W. Jiang, B. Zhang and Z. Ma, *Chem. Sci.*, 2025, **16**, 2453–2464.

26 G. Ye, X. Hong, M. He, J. Song, L. Zhu, C. Zheng, Y. Ma, Y. An, K. Shen, W. Shi, Y. Jia, M. B. Shafqat, P. Gao, D. Xia, F. Chen and Q. Pang, *Adv. Mater.*, 2025, **37**, 2417829.

27 F. Yang, M. Zhang, S. Hong, J. Cao, M. Wang, B. Hong and Y. Lai, *Small*, 2025, **21**, e06662.

28 D. Zhou, M. Zhang, F. Sun, T. Arlt, J. E. Frerichs, K. Dong, J. Wang, A. Hilger, F. Wilde, M. Kolek, M. R. Hansen, P. Bieker, I. Manke, M. C. Stan and M. Winter, *Nano Energy*, 2020, **77**, 105196.

29 S. Tang, W. Guo and Y. Fu, *Adv. Energy Mater.*, 2020, **11**, 2000802.

30 G. Yang, M. L. Lehmann, S. Zhao, B. Li, S. Ge, P.-F. Cao, F. M. Delnick, A. P. Sokolov, T. Saito and J. Nanda, *Energy Storage Mater.*, 2021, **35**, 431–442.

31 C. Wang, T. Yang, W. Zhang, H. Huang, Y. Gan, Y. Xia, X. He and J. Zhang, *J. Mater. Chem. A*, 2022, **10**, 3400–3408.

32 X. Zhang, J. Xie, F. Shi, D. Lin, Y. Liu, W. Liu, A. Pei, Y. Gong, H. Wang, K. Liu, Y. Xiang and Y. Cui, *Nano Lett.*, 2018, **18**, 3829–3838.

33 L. Chen, T. Gu, J. Ma, K. Yang, P. Shi, J. Biao, J. Mi, M. Liu, W. Lv and Y.-B. He, *Nano Energy*, 2022, **100**, 107470.

34 X. Yang, J. Liu, N. Pei, Z. Chen, R. Li, L. Fu, P. Zhang and J. Zhao, *Nano-Micro Lett.*, 2023, **15**, 74.

35 P. Dong, X. Zhang, W. Hiscox, J. Liu, J. Zamora, X. Li, M. Su, Q. Zhang, X. Guo, J. McCloy and M. K. Song, *Adv. Mater.*, 2023, **35**, 2211841.

36 W. Bao, Z. Hu, Y. Wang, J. Jiang, S. Huo, W. Fan, W. Chen, X. Jing, X. Long and Y. Zhang, *Chem. Eng. J.*, 2022, **437**, 135420.

37 Y. Liu, R. Hu, D. Zhang, J. Liu, F. Liu, J. Cui, Z. Lin, J. Wu and M. Zhu, *Adv. Mater.*, 2021, **33**, 2004711.

38 T. Feng, Y. Hu, L. Xu, J. Huang, S. Hu, L. Zhang and L. Luo, *Mater. Today Energy*, 2022, **28**, 101062.

39 W. Yang, Y. Liu, X. Sun, Z. He, P. He and H. Zhou, *Angew. Chem., Int. Ed.*, 2024, **63**, e202401428.

40 D. Hu, G. R. Zhu, P. H. Duan, S. C. Chen, G. Wu and Y. Z. Wang, *Adv. Sci.*, 2025, **12**, 2501012.

41 Y. Bai, Y. Dou, L.-H. Xie, W. Rutledge, J.-R. Li and H.-C. Zhou, *Chem. Soc. Rev.*, 2016, **45**, 2327–2367.

42 S. Wang, M. Wahiduzzaman, L. Davis, A. Tissot, W. Shepard, J. Marrot, C. Martineau-Corcos, D. Hamdane, G. Maurin, S. Devautour-Vinot and C. Serre, *Nat. Commun.*, 2018, **9**, 4937.

43 L. Valenzano, B. Civalleri, S. Chavan, S. Bordiga, M. H. Nilsen, S. Jakobsen, K. P. Lillerud and C. Lamberti, *Chem. Mater.*, 2011, **23**, 1700–1718.

44 H. Furukawa, F. Gándara, Y.-B. Zhang, J. Jiang, W. L. Queen, M. R. Hudson and O. M. Yaghi, *J. Am. Chem. Soc.*, 2014, **136**, 4369–4381.

45 K. Yang, L. Chen, J. Ma, C. Lai, Y. Huang, J. Mi, J. Biao, D. Zhang, P. Shi, H. Xia, G. Zhong, F. Kang and Y. B. He, *Angew. Chem., Int. Ed.*, 2021, **60**, 24668–24675.

46 Q. Wu, M. Fang, S. Jiao, S. Li, S. Zhang, Z. Shen, S. Mao, J. Mao, J. Zhang, Y. Tan, K. Shen, J. Lv, W. Hu, Y. He and Y. Lu, *Nat. Commun.*, 2023, **14**, 6296.

47 P. Martins, A. C. Lopes and S. Lanceros-Mendez, *Prog. Polym. Sci.*, 2014, **39**, 683–706.

48 W. Liu, C. Yi, L. Li, S. Liu, Q. Gui, D. Ba, Y. Li, D. Peng and J. Liu, *Angew. Chem., Int. Ed.*, 2021, **60**, 12931–12940.

49 L. Tian, A. Li, Q. Huang, Y. Zhang and D. Long, *J. Colloid Interface Sci.*, 2021, **586**, 855–865.

50 J. Fu, Z. Li, X. Zhou and X. Guo, *Mater. Adv.*, 2022, **3**, 3809–3819.

51 Q. Liu, G. Yang, X. Li, S. Zhang, R. Chen, X. Wang, Y. Gao, Z. Wang and L. Chen, *Energy Storage Mater.*, 2022, **51**, 443–452.

52 X. Zhang, T. Liu, S. Zhang, X. Huang, B. Xu, Y. Lin, B. Xu, L. Li, C.-W. Nan and Y. Shen, *J. Am. Chem. Soc.*, 2017, **139**, 13779–13785.

53 H. Kwon, H.-J. Choi, J.-k. Jang, J. Lee, J. Jung, W. Lee, Y. Roh, J. Baek, D. J. Shin, J.-H. Lee, N.-S. Choi, Y. S. Meng and H.-T. Kim, *Nat. Commun.*, 2023, **14**, 4047.

54 Y. Yamada, M. Yaegashi, T. Abe and A. Yamada, *Chem. Commun.*, 2013, **49**, 11194.

55 G. Lu, Y. Zhang, J. Zhang, Y. Du, Z. Lv, J. Du, Z. Zhao, Y. Tang, J. Zhao and G. Cui, *Carbon Energy*, 2023, **5**, e287.

56 G. Lu, H. Qiu, X. Du, K. K. Sonigara, J. Wang, Y. Zhang, Z. Chen, L. Chen, Y. Ren, Z. Zhao, J. Du, S. Li, J. Zhao and G. Cui, *Chem. Mater.*, 2022, **34**, 8975–8986.

57 Y. Cui, J. Wan, Y. Ye, K. Liu, L.-Y. Chou and Y. Cui, *Nano Lett.*, 2020, **20**, 1686–1692.

58 Z. Yao, Z. Liu, K. Xia, H. Xie, S. Xie and P. Zhang, *Chem. Sci.*, 2025, **16**, 6812–6821.

59 J. Zhao, M. Hong, Z. Ju, X. Yan, Y. Gai and Z. Liang, *Angew. Chem., Int. Ed.*, 2022, **61**, e202214386.

60 Z. Wang, Z. Sun, Y. Shi, F. Qi, X. Gao, H. Yang, H. M. Cheng and F. Li, *Adv. Energy Mater.*, 2021, **11**, 2100935.

61 J. Zhu, J. Zhang, R. Zhao, Y. Zhao, J. Liu, N. Xu, X. Wan, C. Li, Y. Ma, H. Zhang and Y. Chen, *Energy Storage Mater.*, 2023, **57**, 92–101.

62 J. Zheng, L. Duan, H. Ma, Q. An, Q. Liu, Y. Sun, G. Zhao, H. Tang, Y. Li, S. Wang, Q. Xu, L. Wang and H. Guo, *Energy Environ. Sci.*, 2024, **17**, 6739–6754.

63 J. Lang, Y. Long, J. Qu, X. Luo, H. Wei, K. Huang, H. Zhang, L. Qi, Q. Zhang, Z. Li and H. Wu, *Energy Storage Mater.*, 2019, **16**, 85–90.

64 Z. Zhang, M. Ye, J. Chen, X. Fu, X. Zhou, L. Zheng, L. He, Z. Wu, A. Kumar, L. Li, F. Wan and X. Guo, *Chem. Sci.*, 2025, **16**, 5028–5035.

65 Q. Xu, T. Li, Z. Ju, G. Chen, D. Ye, G. I. N. Waterhouse, Y. Lu, X. Lai, G. Zhou, L. Guo, K. Yan, X. Tao, H. Li and Y. Qiu, *Nature*, 2025, **637**, 339–346.

66 H. Furukawa, K. E. Cordova, M. O'Keeffe and O. M. Yaghi, *Science*, 2013, **341**, 1230444.

67 Y. Gong, C. Yu, Y. Li, J. Qian, C. Wu and Y. Bai, *Batteries*, 2022, **8**, 115.

68 I. Romero-Muñiz, C. Romero-Muñiz, I. del Castillo-Velilla, C. Marini, S. Calero, F. Zamora and A. E. Platero-Prats, *ACS Appl. Mater. Interfaces*, 2022, **14**, 27040–27047.

69 E. Zalnezhad, A. M. S. Hamouda, J. Jaworski and Y. Do Kim, *Sci. Rep.*, 2016, **6**, 33282.

70 F. Pei, Y. Huang, L. Wu, S. Zhou, Q. Kang, W. Lin, Y. Liao, Y. Zhang, K. Huang, Y. Shen, L. Yuan, S. g. Sun, Z. Li and Y. Huang, *Adv. Mater.*, 2024, **36**, 2409269.

71 J. Yu, G. Zhou, Y. Li, Y. Wang, D. Chen and F. Ciucci, *Small*, 2023, **19**, 2302691.

72 X. Wang, S. Huang, K. Guo, Y. Min and Q. Xu, *Adv. Funct. Mater.*, 2022, **32**, 2206976.

73 W. Wang, Y. Yang, J. Yang and J. Zhang, *Angew. Chem., Int. Ed.*, 2024, **63**, e202400091.

74 X.-y. Hu, M.-x. Jing, H. Yang, Q.-Y. Liu, F. Chen, W.-Y. Yuan, L. Kang, D.-H. Li and X.-Q. Shen, *J. Colloid Interface Sci.*, 2021, **590**, 50–59.

75 X. Yi, Y. Guo, S. Chi, S. Pan, C. Geng, M. Li, Z. Li, W. Lv, S. Wu and Q. H. Yang, *Adv. Funct. Mater.*, 2023, **33**, 2303574.

76 L. Wang, S. Yi, Q. Liu, Y. Li, Y. Hu, H. Tu, Y. Wang, A. Sun, F. Zhu, F. Mushtaq, B. Liu, P. Xue, W. Li and M. Liu, *Energy Storage Mater.*, 2023, **63**, 102961.

77 J. Zhang, Y. Zeng, Q. Li, Z. Tang, D. Sun, D. Huang, L. Zhao, Y. Tang and H. Wang, *Energy Storage Mater.*, 2023, **54**, 440–449.

78 S. Lv, X. He, Z. Ji, S. Yang, L. Feng, X. Fu, W. Yang and Y. Wang, *Adv. Energy Mater.*, 2023, **13**, 2302711.

79 F. Tao, K. Yan, C. Dong, J. Wang, Q. Pan, M. Gong, J. Gu, C. Shen, R. Yu, Y. Jiang, Y. Yuan, M. Zhou, M. Huang, X. Xu and L. Mai, *Angew. Chem., Int. Ed.*, 2025, **64**, e202503037.

80 J. Wang, Z. Zhang, J. Han, X. Wang, L. Chen, H. Li and F. Wu, *Nano Energy*, 2022, **100**, 107528.

81 L. Chen, B. Xiao, W. Chen, P. Zhang, T. Huang, W. Huang, Z. Huang, Q. Lin, P. Liu, X. He, Y. Liu, H. Wei, S. Ye, L. Li, J. Chen, X. Yang, X. Ren, X. Ouyang, J. Liu, F. Pan, Q. Zhang and J. Hu, *Nano Energy*, 2024, **131**, 110276.

82 S. Qi, M. Li, Y. Gao, W. Zhang, S. Liu, J. Zhao and L. Du, *Adv. Mater.*, 2023, **35**, 2304951.

83 Z. Song, L. Wang, W. Jiang, M. Pei, B. Li, R. Mao, S. Liu, T. Zhang, X. Jian and F. Hu, *Adv. Energy Mater.*, 2023, **14**, 2302688.

84 Y. Lu, C.-Z. Zhao, J.-Q. Huang and Q. Zhang, *Joule*, 2022, **6**, 1172–1198.

85 C. Li, Y. Lin, J. Liu, F. Ren, Y. Wu, Z. Lv, J. Peng, X. Zheng, Z. Gong and Y. Yang, *Adv. Energy Mater.*, 2024, **14**, 2400985.

86 T. Yang, W. Zhang, Y. Liu, J. Zheng, Y. Xia, X. Tao, Y. Wang, X. Xia, H. Huang, Y. Gan, X. He and J. Zhang, *Small*, 2023, **19**, 2303210.

87 S. Duan, L. Zhang, Y. Zheng, Z. Li, Z. Liu, C. Liao, H. Wang, W. Yan and J. Zhang, *Angew. Chem., Int. Ed.*, 2025, **64**, e202502728.